Research

CrossMark
click for updates

Author for correspondence:
Howard A. Stone
e-mail: hastone@princeton.edu

Fluid-driven cracks in an elastic matrix in the toughness-dominated limit

Ching-Yao Lai[1], Zhong Zheng[1], Emilie Dressaire[2] and Howard A. Stone[1]

[1]Department of Mechanical and Aerospace Engineering, Princeton University, Princeton, NJ 08544, USA
[2]Department of Mechanical and Aerospace Engineering, New York University Tandon School of Engineering, Brooklyn, NY 11201, USA

HAS, 0000-0002-9670-0639

The dynamics of fluid-driven cracks in an elastic matrix is studied experimentally. We report the crack radius $R(t)$ as a function of time, as well as the crack shapes $w(r,t)$ as a function of space and time. A dimensionless parameter, the pressure ratio $\Delta p_f/\Delta p_v$, is identified to gauge the relative importance between the toughness (Δp_f) and viscous (Δp_v) effects. In our previous paper (Lai *et al.* 2015 *Proc. R. Soc. A* **471**, 20150255. (doi:10.1098/rspa.2015.0255)), we investigated the viscous limit experimentally when the toughness-related stresses are negligible for the crack propagation. In this paper, the experimental parameters, i.e. Young's modulus E of the gelatin, viscosity μ of the fracturing liquid and the injection flow rate Q, were chosen so that the viscous effects in the flow are negligible compared with the toughness effects, i.e. $\Delta p_f/\Delta p_v \gg 1$. In this limit, the crack dynamics can be described by the toughness-dominated scaling laws, which give the crack radius $R(t) \propto t^{2/5}$ and the half maximum crack thickness $W(t) \propto t^{1/5}$. The experimental results are in good agreement with the predictions of the toughness scaling laws: the experimental data for crack radius $R(t)$ for a wide range of parameters (E, μ, Q) collapse after being rescaled by the toughness scaling laws, and the rescaled crack shapes $w(r,t)$ also collapse to a dimensionless shape, which demonstrates the self-similarity of the crack shape. The appropriate choice of the viscous or toughness scaling laws is important to accurately describe the crack dynamics.

This article is part of the themed issue 'Energy and the subsurface'.

1. Introduction

The success of hydraulic fracturing for shale gas recovery, i.e. the injection of pressurized water to fracture a shale reservoir and access the trapped natural gas, has motivated much research interest in understanding the underlying mechanisms. Several competing forces involved in the crack dynamics have been identified, such as elastic, viscous and toughness-related stresses [1–3]. The fracturing process of liquid intrusion into elastic solids has also been used to study magma transport, in which the cracks are mainly driven by buoyancy due to the density difference between the injected fluid and rock [4–6].

Hydraulic fractures have been extensively studied theoretically and numerically [2,3,7–10], but experimental observations of the fracture geometry are relatively limited. A summary of the previous experimental work is presented in table 1. Qualitative observations of hydraulic fractures in laboratory experiments were reported by Hubbert & Willis [11]. Experiments were also conducted to study the propagation of fractures, either in a cement block, or along the interface between an acrylic block and a rubber block, as summarized in [18,19]. In some experimental studies on magma-filled cracks, also referred to as buoyancy-driven cracks, gelatin has been used to visualize the fracturing process in an elastic material due to its transparent, elastic and brittle properties [12–14]. Fewer quantitative experiments on the detailed fracture geometry have been reported for hydraulic fractures. Shape measurements of penny-shaped crack tips were performed at a particular time by Bunger [20]. We focus on the experimental developments to obtain the time-dependent information for the fluid-driven crack radius and crack shape in a gelatin matrix, and investigate the dynamics of the crack propagation process in this paper.

Two possible scaling laws can be obtained considering different force balances. When a crack in an elastic solid is created due to the intrusion of a fluid, the fluid pressure balances the elastic stresses at the crack surface, which serves as the driving force for the propagation of hydraulic fractures. The resisting forces during crack propagation include the viscous forces of the flow in the crack, and the forces required to open new crack surfaces in the elastic solid [21]. The viscous-dominated scaling is obtained from the balance between the elastic stresses and the viscous stresses [2], whereas a balance between elastic- and toughness-related stresses gives the toughness-dominated scaling [8,21].

In our previous work, we reported experimental measurement of the time evolution of the crack profile shapes in the viscous-dominated regime [17]. In this paper, we provide the time evolution of crack profile shapes in the toughness-dominated regime, which further allows us to compare the experimental results in the viscous and toughness-dominated regimes. We also identify a dimensionless parameter, the pressure ratio $\Delta p_f/\Delta p_v$, to gauge the relative importance between the toughness and viscous stresses. The importance of the pressure ratio is to determine the proper scaling laws to predict the crack dynamics. For example, the crack size estimated by the toughness scaling law will be an order of magnitude greater than that estimated by the viscous scaling law, if the pressure ratio $\Delta p_f/\Delta p_v \approx 0.03$, as discussed in an example in §5.

The paper is structured as follows: §2 provides a summary of both the viscous and toughness scaling arguments, and the derivation of a dimensionless parameter, the pressure ratio $\Delta p_f/\Delta p_v$ that gauges the viscous and toughness effects. Section 3 explains the experimental method designed to study fluid-driven cracks in the toughness-dominated regime. The experimental results are presented in both dimensional and dimensionless forms in §4. A comparison of experiments in both the viscous- and toughness-dominated regimes, and the significance of identifying the proper regime of a fluid-driven propagating crack are discussed in §5. Concluding remarks are provided in §6.

2. Scaling arguments for fluid-driven cracks

We summarize in this section the scaling arguments for fluid-driven cracks in two asymptotic regimes: viscous and toughness regimes [2,3,8]. We identify a dimensionless parameter, the

Table 1. Summary of previous experimental studies of fluid-driven and buoyancy-driven cracks. We listed the physical mechanisms during crack propagation for each study. $\mathcal{B}$ represents the buoyancy force, $\mathcal{E}$ represents elastic forces, $\mathcal{T}$ indicates the resistance for crack propagation comes from opening the crack tip, while $\mathcal{V}$ indicates that the resistance is from viscous drag of the fluid flow. We emphasized three experimental features: $L(t)$ is the crack length measured as a function of time, $w(r, t^*)$ is the crack shape measured at a certain time t^*, $w(r^*, t)$ is the crack shape measured at a certain position r^* and $w(r, t)$ is the crack shape measured as a function of space and time. '✓' denotes that the information is available from the listed paper and '—' means the information is not reported in the paper. 'H. F.' represents hydraulic fracturing, while 'M. T.' represents magma transport in the column for the motivation.

authors	physical mechanisms		$L(t)$	$w(r, t^*)$	$w(r^*, t)$	$w(r, t)$	motivation
Hubbert & Willis [11]	$\mathcal{E}$		—	—	—	—	H. F.
Takada [12]	$\mathcal{B}, \mathcal{E}$	$\mathcal{T}$	✓	—	—	—	M. T.
Lister & Kerr [5]	$\mathcal{B}, \mathcal{E}$	$\mathcal{V}, \mathcal{T}$	✓	—	—	—	M. T.
Menand & Tait [13]	$\mathcal{B}, \mathcal{E}$	$\mathcal{T}$	✓	—	—	—	M. T.
Kavanagh et al. [14]	$\mathcal{B}, \mathcal{E}$	$\mathcal{V}, \mathcal{T}$	✓	—	—	—	M. T.
Bunger & Detournay [15]	$\mathcal{E}$	$\mathcal{V}, \mathcal{T}$	—	✓	—	—	H. F.
Jeffrey & Bunger [16]	$\mathcal{E}$	$\mathcal{V}$	✓	✓	✓	—	H. F.
Lai et al. [17]	$\mathcal{E}$	$\mathcal{V}$	✓	✓	✓	✓	H. F.
this study	$\mathcal{E}$	$\mathcal{T}$	✓	✓	✓	✓	H. F.

pressure ratio, to determine when the toughness effects are more significant than the viscous effects or vice versa. For the mechanics of crack opening we denote R, W and P, respectively, as the crack radius, the crack maximum half thickness and the scale of fluid pressure in the crack, which balances the elastic stress applied on the crack surface. Also, E is Young's modulus, σ is Poisson's ratio and $2\gamma_s$ is the energy per unit area required to open new crack surfaces in the elastic solid.

(a) Toughness and viscous scaling arguments

When a crack is opened in an elastic medium due to the intrusion of fluid, the magnitude of the fluid pressure, which balances the elastic stress (equation (A 1)) exerted on the crack surface, is

$$P \approx \frac{E}{2(1 - \sigma^2)} \frac{W}{R}. \tag{2.1}$$

A crack propagates when $K_I = K_{Ic}$ [22] (see appendix A), where $K_I \approx 2\sqrt{R/\pi}P$ is the mode I stress intensity factor for a penny-shaped crack (equation (A 2)) and $K_{Ic} = \sqrt{2E\gamma_s}$ is the fracture toughness [13,23], which is a material property that represents the resistance of a material to the opening of new crack surfaces. Thus, the typical fluid pressure P, or the elastic stress, for a crack radius R in a material dominated by the toughness of opening the crack is

$$P \approx \sqrt{\frac{\pi \gamma_s E}{2R}}. \tag{2.2}$$

For the fluid flow in the crack, lubrication theory can be applied due to the narrow geometry of the crack ($W \ll R$), as inertial effects are expected to be small. Viscous stresses cause a radial pressure gradient in the flow. In this viscous-dominated flow limit, the change of crack thickness W with time can be shown [2] to scale as

$$\frac{W}{t} \approx \frac{1}{3\mu} \frac{W^3 P}{R^2}. \tag{2.3}$$

Table 2. Summary of the scaling laws in both the viscous and the toughness regimes. E is the Young modulus of the elastic matrix, μ is the viscosity of the fracturing liquid, Q is the injection flow rate, $2\gamma_s$ is the energy per unit area needed to create new crack surfaces and σ is the Poisson ratio. R, W and P denote, respectively, the approximate crack radius, half width and fluid pressure of the growing crack.

regime	viscous regime	toughness regime
crack radius	$R \approx \left(\dfrac{Q}{4\pi}\right)^{1/3}\left(\dfrac{E}{6\mu(1-\sigma^2)}\right)^{1/9} t^{4/9}$	$R \approx \left(\dfrac{EQ^2}{32(1-\sigma^2)^2\pi^3\gamma_s}\right)^{1/5} t^{2/5}$
crack thickness	$W \approx \left(\dfrac{Q}{4\pi}\right)^{1/3}\left(\dfrac{E}{6\mu(1-\sigma^2)}\right)^{-2/9} t^{1/9}$	$W \approx \left(\dfrac{(1-\sigma^2)^4\pi Q\gamma_s^2}{E^2}\right)^{1/5} t^{1/5}$
fluid pressure	$P \approx \dfrac{E}{2(1-\sigma^2)}\left(\dfrac{E}{6\mu(1-\sigma^2)}\right)^{-1/3} t^{-1/3}$	$P \approx \left(\dfrac{(1-\sigma^2)\pi^4 E^2\gamma_s^3}{Q}\right)^{1/5} t^{-1/5}$

The relation between the crack radius R and the maximum thickness $2W$ is set by the global volume conservation (equation (A 4)):

$$4\pi R^2 W \approx Qt, \tag{2.4}$$

where Q is the injection flow rate of the fracturing liquid.

In the viscous-dominated regime, the elastic stresses on the crack (equation (2.1)) balance the fluid pressure in the viscous flow (equation (2.3)), and the toughness effects of the elastic material are assumed negligible. By contrast, in the toughness-dominated regime, there is a balance between the fluid pressure, or the elastic stresses, set by the elastic strain (equation (2.1)) and the fracture toughness (equation (2.2)), while the viscous effects are assumed negligible. Thus, the scaling laws for the time dependence of R, W and P in the viscous and toughness regimes can be obtained using equations (2.1), (2.3), (2.4) and (2.1), (2.2), (2.4), respectively, as summarized in table 2.

(b) Pressure ratio

To examine the viscous effects, which are neglected in the toughness regime, we compare the typical toughness-related stress $\Delta p_f \approx \sqrt{\gamma_s E/R}$ (equation (2.2) without the respective coefficients) to the typical viscous stress $\Delta p_v \approx \mu Q/W^3$ (equations (2.3) and (2.4) without the constant coefficients). A dimensionless parameter, the pressure ratio $\Delta p_f/\Delta p_v$, can be identified to gauge the relative importance of the toughness and viscous effects [8,17],

$$\frac{\Delta p_f}{\Delta p_v} = \frac{\gamma_s^{1/2}E^{1/2}W^3}{\mu Q R^{1/2}}. \tag{2.5}$$

If we substitute in the time-dependent toughness-dominated scaling laws for R and W (table 2) and drop the constant coefficients, equation (2.5) becomes

$$\left[\frac{\Delta p_f}{\Delta p_v}\right]_t = \frac{(1-\sigma^2)^{13/5}\gamma_s^{9/5}t^{2/5}}{\mu Q^{3/5}E^{4/5}}. \tag{2.6}$$

By contrast, if we substitute the viscous-dominated scaling laws for R and W into equation (2.5), we obtain the pressure ratio

$$\left[\frac{\Delta p_f}{\Delta p_v}\right]_v = \left[\frac{\Delta p_f}{\Delta p_v}\right]_t^{5/18}, \tag{2.7}$$

which is also consistent with the dimensionless toughness and viscosity defined by Savitski & Detournay [8]. To be self-consistent, we use $[\Delta p_f/\Delta p_v]_t$, as defined in equation (2.6), only when the toughness scaling laws are valid, which implies $[\Delta p_f/\Delta p_v]_t \gg 1$. In the viscous-dominated regime where $[\Delta p_f/\Delta p_v]_t \ll 1$, it is more consistent to use the viscous scaling laws and hence $[\Delta p_f/\Delta p_v]_v$

to estimate the pressure ratio (see eqn. (B 2) in Lai *et al.* [17]) and evaluate the relative importance of toughness to viscous effects. For all of the experiments reported in §3 $[\Delta p_f/\Delta p_v]_t > 10^3$.

3. Experimental design for the toughness-dominated regime

To conduct experiments on fluid-driven cracks in an elastic medium in the toughness-dominated regime, we tune the parameters E, Q and μ so that $[\Delta p_f/\Delta p_v]_t \gg 1$, as shown in table 3. The goal of the experiments is to visualize the time evolution of the shape of the crack $w(r,t)$ and the propagation of the crack radius $R(t)$. We have previously reported extensive experimental results in the viscous-dominated regime [17]. Compared with the experimental set-up designed for the viscous-dominated regime, for the toughness-dominated experiments reported here, we added a long tube, which was connected to a syringe to precisely calibrate the injection flow rate of the fracturing liquid. The details of the method are described below.

(a) Method

A transparent block of solid gelatin was prepared as the elastic matrix to be fractured. This material has been used in several fluid-driven fracture experiments [12–14,24]. Young's modulus of the matrix can be changed by varying the concentration of the gelatin powder (Gelatin type A, ThermoFisher Scientific, USA), and Young's modulus was measured using the indentation method [17,25]. A long tube was connected to a syringe and a needle, which was placed inside the gelatin (figure 1a). The syringe and part of the tube were filled with air, while the rest of the tube and the needle were filled with the fracturing liquid (water or mineral oil). At the beginning of the injection process, the air–liquid interface was stationary, and the air was compressed. When a threshold air pressure was reached, the air–liquid interface started to move (shown by the red arrow in figure 1a) and reached the speed calculated from the injection rate Q set by the syringe pump (Harvard apparatus, PhD Ultra) within a 7% error. A USB IDS uEye camera (1280 × 1024 pixels, frame rate = 10 fps) was placed on top of the block and a Nikon D5100 camera (640 × 424 pixels, frame rate = 29 fps) was placed on the side to record the three-dimensional shape of the crack. The camera configuration is shown in figure 1a and typical side and top views of a growing crack are shown in figure 1b,c.

When the liquid enters the solid matrix, it creates a penny-shaped crack. We define time zero as the moment when the liquid, dyed red for visualization as shown in figure 1, appears at the tip of the needle. The error from this determination is ±0.5 s. In table 3, we summarize the typical values of μ, E and Q used in our experiments. The viscosity μ varied by a factor of 27, E by a factor of 8 and Q by a factor of 30. We used $\gamma_s \approx 1\,\mathrm{J\,m^{-2}}$ measured by Menand & Tait [13]. In the calculation of the pressure ratio (equation (2.6)), t is chosen to be the time half-way through the experiments. The pressure ratio $[\Delta p_f/\Delta p_v]_t \approx 10^3 - 10^4$ in our experiments, which confirms that the experiments are in the toughness-dominated regime.

In all our experiments, the buoyancy effects from the density difference between the fracturing liquid and the elastic solid are negligible. For example, in a typical experiment, the crack radius is $R \approx 2\,\mathrm{cm}$, the density difference is $\Delta\rho \approx 900\,\mathrm{kg\,m^{-3}}$ and the gelatin Young's modulus is $E \approx 20\,\mathrm{kPa}$. Consequently, we can estimate the typical buoyancy-related stress to be $\Delta\rho g R \approx 180\,\mathrm{Pa}$, and the toughness-related stress is $\Delta p_f \approx \sqrt{\gamma_s E/R} \approx 10^3\,\mathrm{Pa}$. Thus, the buoyancy effects are negligible in the experiments. In addition, the viscous drag from flow along the needle and the long tube is also negligible compared with the toughness-related stresses. For example, given the inner radius (R_{in}) and the length (L) of the needle and tube (figure 1), $\mu \approx 26.9\,\mathrm{mPa\,s}$ and $Q \approx 1\,\mathrm{ml\,min^{-1}}$, the viscous stresses from the flow along the needle and the tube is estimated to be $\mu Q L/(R_{in})^4 \approx 88\,\mathrm{Pa}$, which is negligible compared with the typical toughness-related stresses $\Delta p_f \approx 10^3\,\mathrm{Pa}$. An experimental verification of the lack of significant needle-size effects is also provided in appendix C.

To estimate the plastic effects, we calculate the size of the process zone r_p at the crack tip where the inelastic deformation occurs. For a gelatin of a typical yield stress $\tau_y \approx 10^4 - 10^5\,\mathrm{Pa}$ [26],
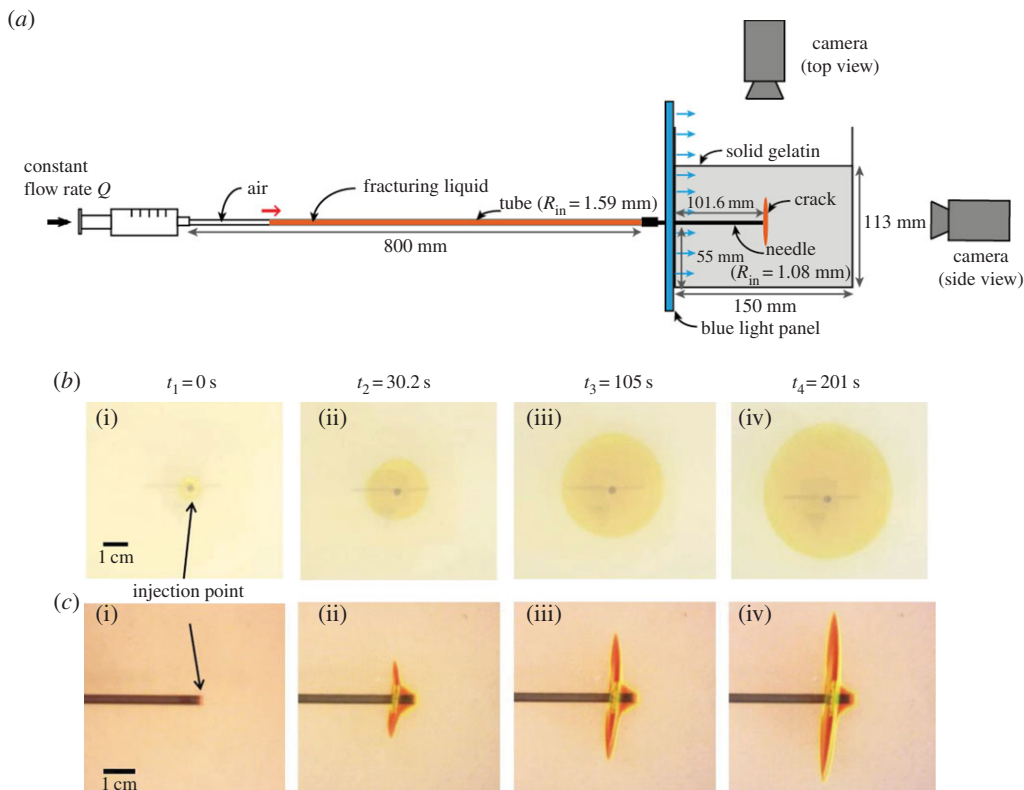
6

rsta.royalsocietypublishing.org   Phil. Trans. R. Soc. A **374**: 20150425

(a)

camera (top view)

constant flow rate Q

air — fracturing liquid — tube ($R_{in} = 1.59$ mm)

solid gelatin

101.6 mm — crack

800 mm

55 mm — needle ($R_{in} = 1.08$ mm)

113 mm

camera (side view)

150 mm — blue light panel

(b) $t_1 = 0$ s $t_2 = 30.2$ s $t_3 = 105$ s $t_4 = 201$ s

(i)   (ii)   (iii)   (iv)

1 cm

injection point

(c)   (i)   (ii)   (iii)   (iv)

1 cm

Figure 1. (a) Schematic of the experimental set-up. A needle connected to a long tube is inserted into a block of elastic gelatin. The long tube and the needle are filled with the fracturing liquid. An air–liquid interface in the long tube is used to calibrate the flow rate of the liquid. A syringe filled with air first compresses the air column, then pushes the liquid forward to create a penny-shaped crack inside the gelatin block. The direction of liquid flow is marked by the arrow above the air–liquid interface. A blue light panel, facing the camera, was placed behind the crack for visualization purposes. (b) The side view and (c) top view of a penny-shaped crack. $t = 0$ is defined as the time when the fracturing liquid emerges from the needle tip. The flow rate at which the fracturing liquid is injected is $Q = 1$ ml min^{-1}, the fracturing liquid is water (mixed with fluorescein and red dye) and Young's modulus of the gelatin matrix is $E = 77 \pm 7.7$ kPa. R_{in} represents inner radius.

Table 3. The experimental parameters and the pressure ratios for all experiments in the toughness-dominated regime. The pressure ratio is time-dependent (defined in equation (2.6)) and we chose t to be the time half way through the experiments. The viscosities of the mineral oils were measured using a rheometer (Physica MCR 301). We use a standard value for the viscosity of water. Water is mixed with fluorescein and red dye, while mineral oils are mixed with fluorescein only.

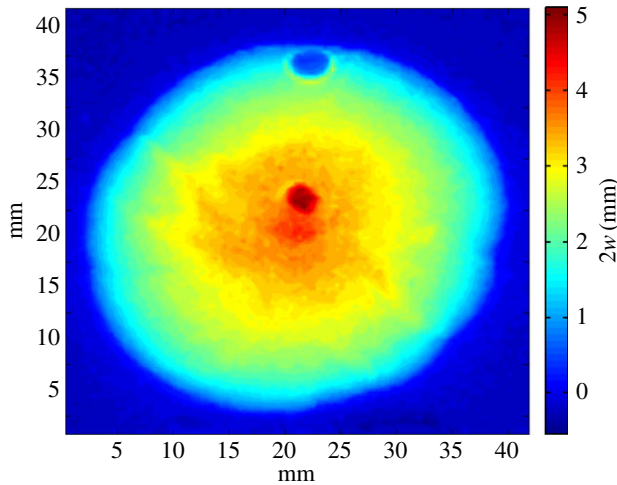| fracturing liquid	viscosity μ (mPa s)	Young's modulus E (kPa)	injection rate Q (ml min^{-1})	pressure ratio $[\Delta p_f / \Delta p_v]_t$
water	1	74 ± 7.4	1 ± 0.07	1.8×10^4
water	1	24 ± 2.4	1 ± 0.07	4.3×10^4
water	1	16 ± 1.6	1 ± 0.07	6.4×10^4
water	1	55 ± 5.5	1 ± 0.07	2.3×10^4
water	1	120 ± 12	3 ± 0.21	4.1×10^3
mineral oil	11.5 ± 0.2	21 ± 2.1	0.5 ± 0.04	8.9×10^3
mineral oil	26.9 ± 0.1	21 ± 2.1	0.1 ± 0.007	1.9×10^4

Figure 2. The thickness distribution ($2w$) of the entire crack measured at $t = 116$ s. Experimental parameters: $\mu = 11.5 \pm 0.2$ Pa s, $E = 77 \pm 7.7$ kPa and $Q = 1$ ml min^{-1}. We note that the signal at the centre of the crack was blocked by the needle.

assuming $K = K_{IC}$, the process zone $r_p \approx K^2/\tau_y^2 \approx K_{IC}^2/\tau_y^2 \approx 2E\gamma_s/\tau_y^2 \approx 0.4\,\mu\text{m}$–0.4 mm, which is much smaller than the representative crack radius $R \approx 20$ mm in our experiments. Thus, the plastic effects are negligible for the experiments of the current paper.

(b) Measurement of crack shape

The advantage of using transparent gelatin is that we can visualize the shape of the crack. We used Bunger's [20] imaging technique, measuring the change of light intensity as light passes through the liquid-filled crack, to obtain the time-dependent crack thickness $w(r, t)$ [17]. This technique has been used previously to obtain the crack thickness for a penny-shaped crack [15,20] and for a saucer-shaped crack near a free surface [27].

We set a uniform blue light background of light intensity I_0 behind the crack, dye the fracturing liquid with fluorescein (15 µl fluorescent yellow 131 SC, Keystone +10 g fracturing liquid) and measure the intensity of light I after it passes through the liquid-filled crack. We calibrate the change of the blue light intensity (I/I_0), as it travels through the fluorescein-filled liquid, as a function of liquid thickness d. Thus, we are able to convert the information of the measured blue light intensity I to the crack thickness $2w$ (for technical details, see [17]). A typical result is shown in figure 2.

4. Results and observations

Once the liquid enters the solid matrix, it creates a penny-shaped crack (see figure 1b, c for the side and top views, respectively). The thickness of a crack $2w$ at any given time can be obtained using the imaging technique described in §3b, as shown in figure 2. We will show in this section the time dependence of both the crack radius $R(t)$ and the crack shape $2w(r, t)$, and the dimensionless data rescaled by the toughness scaling laws (table 2).

(a) Dimensional results

We measured the radius of the crack as a function of time $R(t)$ for various liquid viscosities μ, Young's moduli E and injection flow rates Q. The results are shown in figure 3a. We chose carefully the experimental parameters so that $4 \times 10^3 \leq [\Delta p_f/\Delta p_v]_t \leq 6 \times 10^4$ (table 3); thus, the viscous effects are negligible. The results show that the crack radius R exhibits a power-law dependence on time, as shown in the log–log plot (figure 3a).
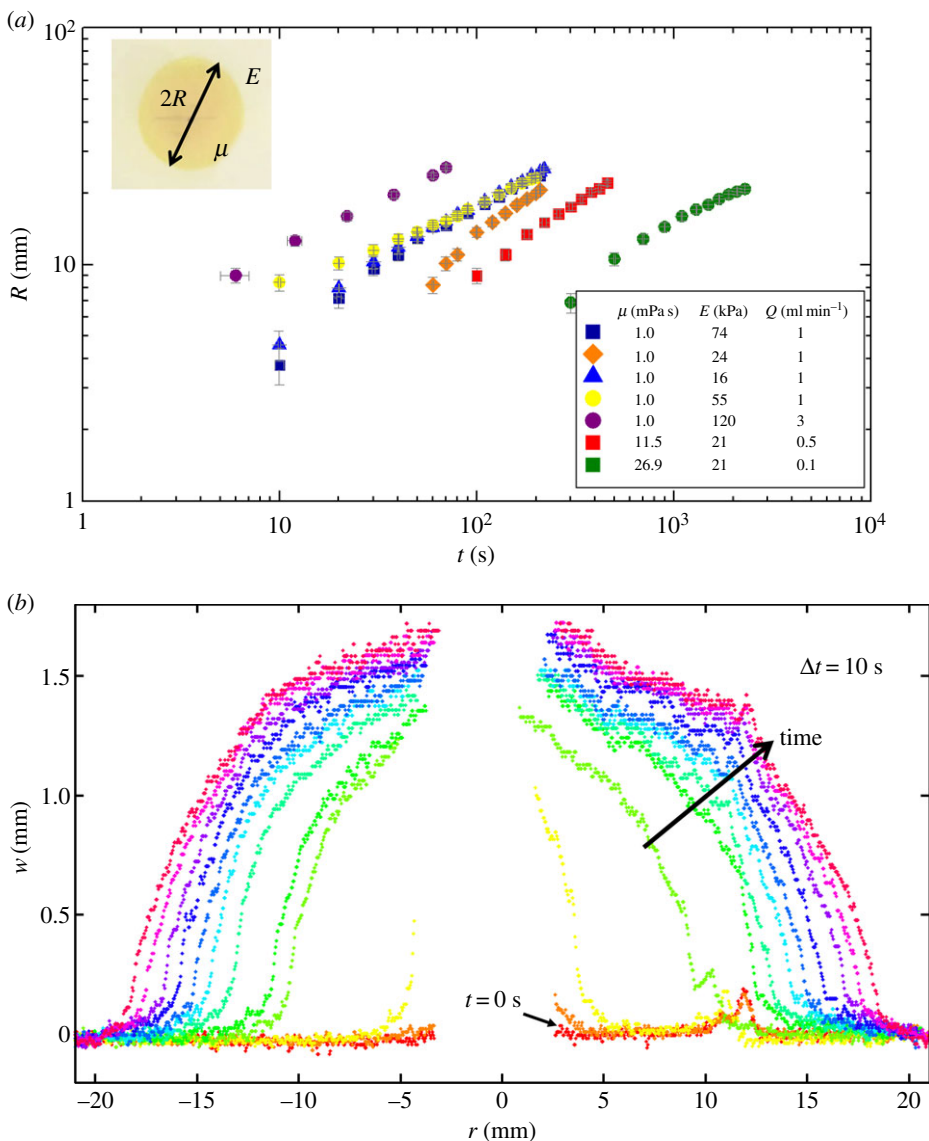
Figure 3. (a) Crack radius $R(t)$ as a function of time for various values of μ, E and Q. (b) The time evolution of the crack profile shapes $w(r, t)$. Each curve is the crack profile measured at a fixed cross section. The time difference Δt between two adjacent curves is 10 s. The flat curve at the bottom corresponds to $t = 0$. Note that $r = 0$ is defined at the centre of the crack, where the light is blocked by the needle and no data were recorded. Experimental parameters: $\mu = 11.5 \pm 0.2$ Pa s, $E = 77 \pm 7.7$ kPa and $Q = 1$ ml min^{-1}.

Also, for a given experiment we report the crack half thickness profile $w(r, t)$ at a cross section through the centre of the crack, as shown in figure 3b. The red flat curve represents the crack profile at $t = 0$ and the crack profiles are measured every 10 s. For all curves there is a region at the centre of width 6 mm, where the light signal is blocked by the needle.

(b) Dimensionless results

To compare the results $R(t)$ and $w(r, t)$ with the toughness scaling laws, we rescaled the raw experimental data in figure 3a,b by the toughness scaling laws provided in table 2. When the
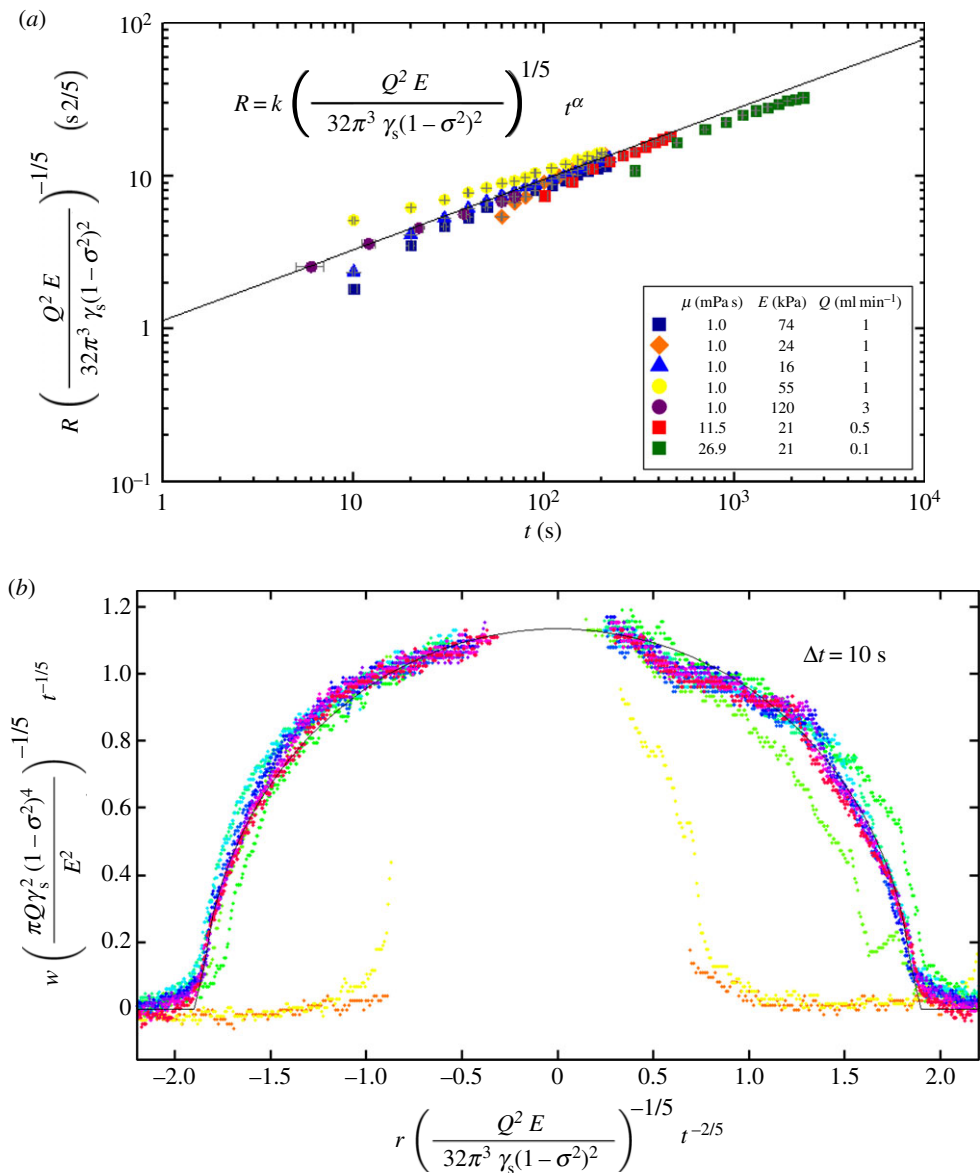
Figure 4. (*a*) The rescaled crack radius using the toughness scaling arguments in table 2. The collapse of experimental data supports the toughness scaling laws. We fit each rescaled curve at late times with a power-law form (see the equation shown on the plot) and obtain an average pre-factor $k = 1.14 \pm 0.35$ and exponent $\alpha = 0.46 \pm 0.06$. The power-law curve with an average k and α is shown by the dark line. (*b*) The dimensionless crack profiles, in which r is rescaled by R and w is rescaled by W. The black curve represents the best elliptical fit, equation (4.1), where $A \approx 0.61$. The asymptotic solution in equation (B 10) gives $A \approx 0.47$ and the difference in A is likely due to the uncertainties in measuring E, Q, w, r, t and the values of γ_s, σ used in this paper. The convergence of the dimensionless crack shapes to a universal shape demonstrates the self-similarity of the crack shapes.

data are rescaled using the scaling laws in table 2, good collapse of the rescaled crack radius was obtained, as shown in figure 4a. We fit each rescaled experimental curves with a power-law function, and obtain an average pre-factor $k = 1.14 \pm 0.35$ and exponent $\alpha = 0.46 \pm 0.06$, which shows a good agreement with the toughness scaling law.
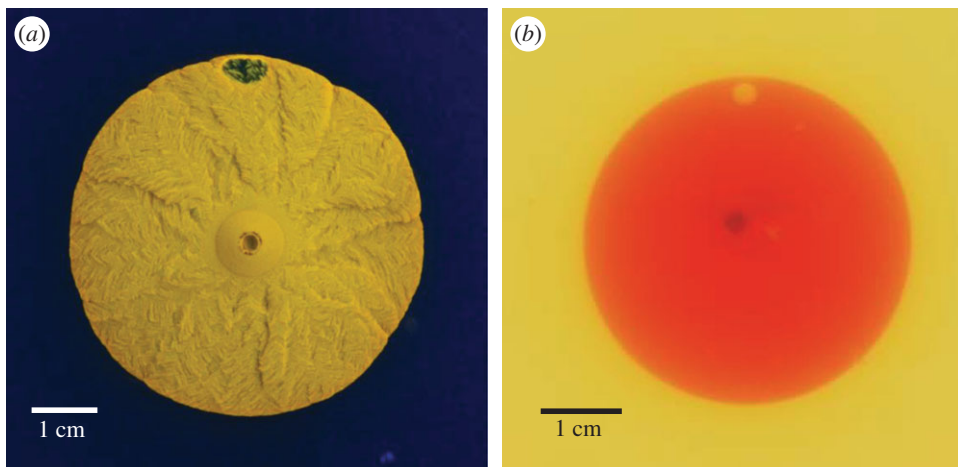
Figure 5. (a) The roughness of a crack surface is visualized using a higher concentration of fluorescein (200 µl fluorescent yellow 131 SC, Keystone +10 g mineral oil) in the fracturing liquid than the concentration used for the crack shape measurement. The crack surface appears to be rough when we use mineral oils as the fracturing liquid. The fracturing liquid in this figure is mineral oil of viscosity $\mu = 11.5$ mPa s. The direction of the excitation blue light is into the page. (b) The crack surface appears to be smooth when the injected liquid is water (dyed red).

We next rescale the time-dependent crack profile shapes (figure 3b). Since the dependence of both the crack radius R and maximum half thickness W on time is available (table 2), we can rescale r and $w(r,t)$ using the scaling laws for R and W. Here, instead of $\gamma_s \approx 1$ J m^{-2}, we use $\gamma_s \approx 5.15$ J m^{-2} determined by fitting the crack radius R with the theoretical prediction in equation (B 8). We obtained convergence of the dimensionless profile shapes to a universal dimensionless crack shape after around 30 s, as shown in figure 4b. The collapse of the crack shapes suggests that the profile shapes are self-similar.

We also fit the dimensionless crack shapes with an elliptical functional form (to be consistent with the theoretical prediction, equation (B 10)):

$$\frac{w}{W_c} = A \left[\left(\frac{3\pi}{2} \right)^{4/5} - \left(\frac{r}{R_c} \right)^2 \right]^{1/2} \tag{4.1}$$

and obtained $A \approx 0.61$, as shown in the black curve in figure 4b. The asymptotic solution in equation (B 10) gives $A = (64/3\pi^6)^{1/5} \approx 0.47$. We note that there is a 23% difference for the value A between the theoretical prediction and the fit of experimental data. This is likely to be due to the measurement errors for Young's modulus of gelatin E, injection flow rate Q, crack thickness $w(r,t)$ and the value of Poisson's ratio σ and $2\gamma_s$ used in the paper. In addition, the difference may also come from the higher order effects for the theoretical prediction, and other effects we did not consider in the theory, such as the plasticity and nonlinearity effects.

(c) Crack roughness

We note that for water as the fracturing liquid, the crack surface appeared smooth, while with mineral oils as the fracturing liquid, the crack surface appeared rough. The detailed structure of a rough crack surface with mineral oils as the fracturing liquid can be clearly observed, as shown in figure 5a, as we change the direction of illumination (the direction of the excitation blue light is into the page) and increase the dye concentration (200 µl fluorescent yellow 131 SC, Keystone +10 g mineral oil). In comparison, figure 5b shows a smooth crack surface with water as the fracturing liquid.
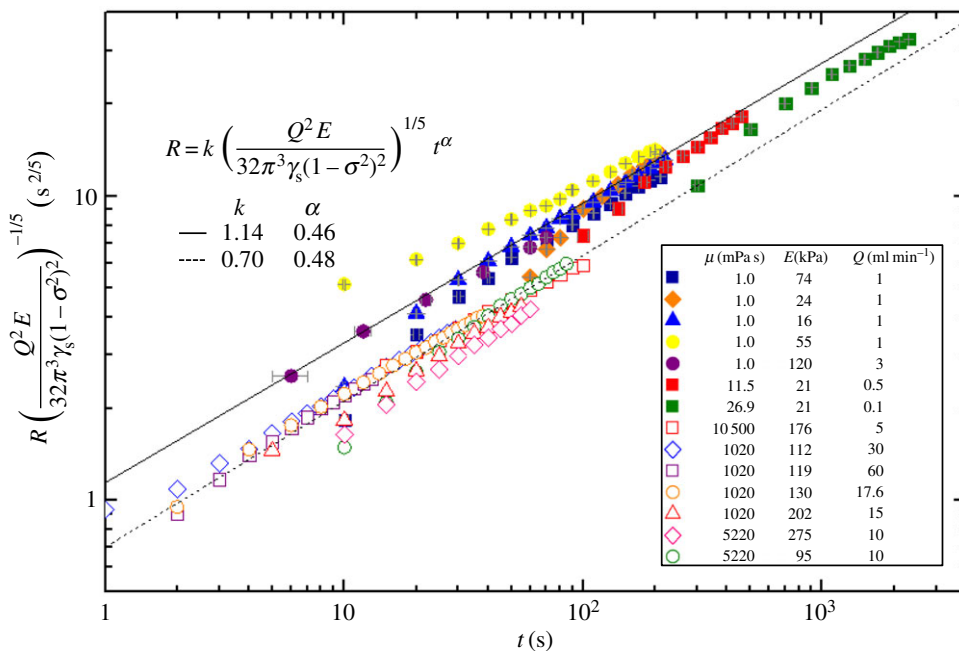
Figure 6. A comparison of the experimental data between the toughness and the viscous regimes, both rescaled by the toughness scaling laws. The data in the viscous regime, where $0.62 < [\Delta p_f / \Delta p_v]_v < 0.97$, were adapted from reference [17] and shown with the empty symbols. The data in the toughness regime, where $4.1 \times 10^3 < [\Delta p_f / \Delta p_v]_t < 6.4 \times 10^4$, are shown with solid symbols. We note that the functional form of the viscous and toughness scaling laws (table 2) are very similar, thus the toughness scaling laws also seem to collapse the data in the viscous regime. However, there is a gap in the pre-factor from fitting the toughness and viscous datasets. The toughness data suggest an average pre-factor $k = 1.14 \pm 0.35$ (solid line), while the viscous data suggest an average pre-factor $k = 0.7 \pm 0.14$ (dashed line).

5. Discussion

In §4, we have shown the self-similarity of the time evolving crack shapes. In addition, there is good agreement between the experimental results and the predictions of the scaling laws in the toughness-dominated limit. Similar procedures had been developed by Lai *et al.* [17] for the experiments and scaling laws in the viscous-dominated regime. Now we compare the toughness data $[\Delta p_f / \Delta p_v]_t \gg 1$, with the viscous data $[\Delta p_f / \Delta p_v]_v < 1$.

We plotted the time-dependent crack radius $R(t)$ from experiments in both the viscous and toughness regimes, both rescaled by the toughness scaling laws, as shown in figure 6. We observe that the functional forms of the viscous and toughness scaling laws are very similar in terms of time dependence ($t^{4/9}$ and $t^{2/5}$, respectively), and the dependence on μ, E and Q shows modest differences (table 2). Given these similarities in the functional forms, within the parameter limits of our experimental system the toughness scaling law seems to collapse the experimental data in both the viscous and toughness regimes.

Another important issue is that the pre-factors in the power-law forms are different between our experimental data in the viscous and toughness regimes. In particular, for experimental data in the toughness limit, the pre-factor is $k = 1.14 \pm 0.35$, as shown by the solid line in figure 6. By contrast, for experimental data in the viscous regime, the pre-factor is $k = 0.7 \pm 0.14$, as shown by the dashed line in figure 6.

However, an experiment in the viscous limit with an extremely small pressure ratio will do less well in collapsing the viscous data in figure 6, when rescaled by the toughness scaling law. This feature is because the crack radius predicted by the viscous and toughness scaling laws, denoted

by R_v and R_t, respectively, vary with the pressure ratio according to

$$\frac{R_v}{R_t} \approx \left[\frac{\Delta p_f}{\Delta p_v} \right]_v^{2/5} = \left[\frac{\Delta p_f}{\Delta p_v} \right]_t^{1/9} , \tag{5.1}$$

though the exponent is small. An improper choice of scaling laws will give a larger discrepancy between the theoretical and experimental results when the pressure ratio is very different from unity. For example, consider a model hydraulic fracturing system where the typical Young's modulus of shale $E = 40$ GPa, fracture toughness $K_{Ic} = 0.5$ MPa m$^{-1/2}$, Poisson's ratio $\sigma = 0.25$, fracturing liquid viscosity $\mu = 0.5$ Pa s and constant injection flow rate $Q = 0.08$ m^3 s^{-1}. About 1 h after the fracture grows, the system is in the viscous regime as the pressure ratio is $[\Delta p_f/\Delta p_v]_v \approx 0.03$. If we use the toughness scaling, we predict the crack size to be approximately 260 m long, while the viscous scaling predicts only 95 m. Thus, choosing the appropriate scaling law is essential to provide a good estimate for the dynamics of crack propagation.

6. Conclusion

A laboratory experiment was developed to study fluid-driven cracks inspired by the process of hydraulic fracturing. Two possible sets of scaling arguments, the viscous and toughness scalings, were discussed, considering whether the resistance of crack propagation is from the viscous stresses or the toughness-related stresses. In our previous work [17], we chose gelatin as an analogue for rocks and investigated the dynamics of fluid-driven cracks in the viscous-dominated regime. In this paper, we redesigned the experiments to study the crack dynamics in the toughness-dominated regime. Time-dependent information of the crack radius $R(t)$ and crack shape $w(r, t)$ were obtained in our experiments, and the dimensional data were rescaled based on the toughness scaling laws. The collapse of dimensionless data for a wide range of experimental parameters (E, Q, μ) demonstrates the success of the toughness scaling arguments.

In particular, the pressure ratio (equation (2.5)), a dimensionless parameter defined as the ratio of toughness-related stresses to viscous stresses, is identified to be a guideline for the choice of the appropriate scaling laws to describe the crack propagation. We note that the difference between the predictions for the crack size in the viscous- and toughness-dominated regimes can be significant when the pressure ratio departs from unity.

Our experimental system provides an idealized model to study fluid-driven fracturing operations such as hydraulic fracturing. Alternative experimental models, considering the heterogeneity of the rocks, the leak-off of liquid from the cracks, the effects of proppants in the fluid flow and the porelastic effects of the solid matrix, could be potentially explored from proper modifications of the experimental system. We hope to report some of these studies in future work.

Appendix A. Governing equations in the toughness-dominated regime

Let us consider an axisymmetric penny-shaped crack in an infinite elastic medium. We define $r = 0$ at the centre of the crack and $r = R(t)$ at the crack radius. The z-axis is aligned with the axial direction. We assume the shear traction on the crack surface is small compared with the normal

traction. The elastic stress $\sigma_{zz} = -p(r,t)$ is related to the shape of the crack by [2]

$$p(r,t) = -\frac{E}{2(1-\sigma^2)} \int_0^{R(t)} M\left(\frac{r}{s}\right) \frac{\partial w(s,t)}{\partial s} \frac{ds}{s},$$ (A 1)

where w is the half crack thickness and M is a kernel defined by Spence & Sharp [2].

In the realm of linear elastic fracture mechanics, the stress singularity at the crack tip can be characterized by the stress intensity factor. The mode I stress intensity factor for a penny-shaped crack is Rice [21]:

$$K_I = \frac{2}{\sqrt{\pi R}} \int_0^{R(t)} \frac{p(r,t)}{\sqrt{R^2 - r^2}} r \, dr.$$ (A 2)

Irwin [22] showed that a crack propagates when K_I reaches a critical value K_{Ic}, the fracture toughness which characterizes the difficulty in opening new crack surfaces in a material.

$$K_I = K_{Ic}.$$ (A 3)

The fracture toughness K_{Ic} is a property of the elastic material [6] which can be measured experimentally [13].

Lastly, the fluid flow inside the crack is incompressible, and thus the crack volume is equal to the volume of fracturing liquid supplied at flow rate Q,

$$4\pi \int_0^{R(t)} rw(r,t) \, dr = Qt.$$ (A 4)

The scaling argument based on equations (A 1)–(A 4) can be obtained. This scaling argument (toughness limit) is different from the scaling argument in Lai *et al.* [17], which is in the viscous limit. Both the viscous and toughness scaling arguments are summarized in table 2.

Appendix B. Crack shape in the toughness-dominated regime

In this section, we provide an approximate solution for the crack shape and front location in the toughness regime. We first note that the equation for the pressure distribution (A 1) can also be rewritten as a double integral equation (e.g. [8,28])

$$w(r,t) = \frac{4R(1-\sigma^2)}{\pi E} \int_{r/R}^1 \frac{\xi}{\sqrt{\xi^2 - (r/R)^2}} \int_0^1 \frac{xp(x\xi R,t)}{\sqrt{1-x^2}} \, dx \, d\xi.$$ (B 1)

In the toughness regime, the fluid flow within the crack is quasi-steady. The fluid pressure within the crack is only a function of time (independent of space). We denote the pressure as $p_s(t)$, and from equation (B 1), we obtain the elliptical crack shape

$$w(r,t) = \frac{4R(1-\sigma^2)p_s}{\pi E} \left[1 - \left(\frac{r}{R}\right)^2\right]^{1/2}.$$ (B 2)

We note that at this time, the time-dependent functional forms of $p_s(t)$ and $R(t)$ are yet to be determined.

In the toughness regime, given that the pressure $p_s(t)$ is only time dependent, the crack propagation criterion (A 3) and the stress intensity factor (A 2) can be rewritten to provide an explicit expression for pressure $p_s(t)$ as a function of crack radius $R(t)$:

$$p_s(t) = \frac{\pi^{1/2}K_{IC}}{2R^{1/2}}.$$ (B 3)

14

rsta.royalsocietypublishing.org *Phil. Trans. R. Soc. A* **374**: 20150425
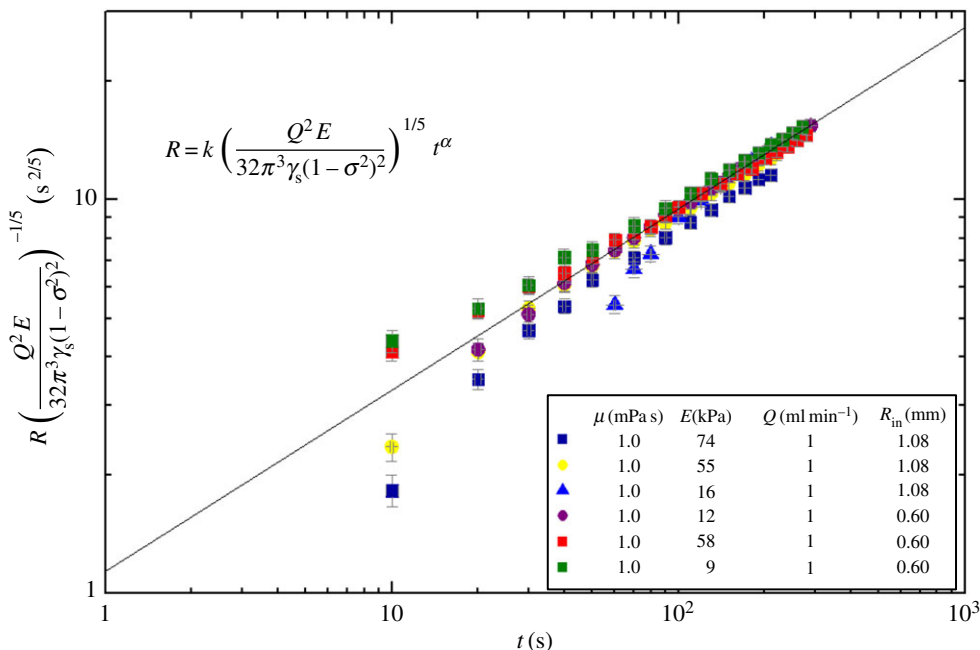

Figure 7. The effects of needle size on the dimensionless crack radius versus time. R_{in} represents the inner radius of the needle. The collapse of experimental data indicates that the effects of the needle size are not important in our experiments. The dark line is the same line as shown in figure 4a with $k \approx 1.14$ and $\alpha \approx 0.46$.

We now combine (B 2) and (B 3) to obtain an expression for the crack half thickness $w(r, t)$ with only $R(t)$ to be determined:

$$w(r,t) = \frac{2K_{IC}(1-\sigma^2)}{\pi^{1/2}E}R^{1/2}\left[1-\left(\frac{r}{R}\right)^2\right]^{1/2}. \tag{B 4}$$

Then, we can substitute the profile shape (B 4) into the global mass constraint (A 4), and we obtain the time evolution of the crack radius $R(t)$:

$$R(t) = \left[\frac{9EQ^2}{128\pi(1-\sigma^2)^2\gamma_s}\right]^{1/5} t^{2/5}. \tag{B 5}$$

Once the location of crack tip $R(t)$ is known, we can substitute (B 5) into (B 3) to obtain the liquid pressure inside the crack:

$$p_s(t) = \left[\frac{2\pi^3(1-\sigma^2)E^2\gamma_s^3}{3Q}\right]^{1/5} t^{-1/5}; \tag{B 6}$$

we can also substitute (B 5) into (B 4) to obtain the time evolution of the crack shape:

$$w(r,t) = \left(\frac{48}{\pi^4}\right)^{1/5}\left[\frac{\pi(1-\sigma^2)^4Q\gamma_s^2}{E^2}\right]^{1/5}\left[1-\left(\frac{r}{R}\right)^2\right]^{1/2} t^{1/5}. \tag{B 7}$$

From the scaling arguments in the toughness regime presented in table 2, we can define the characteristic scales for the pressure P_c, crack thickness W_c and radius R_c

$$R_c \approx \left[\frac{EQ^2}{32\pi^3(1-\sigma^2)^2\gamma_s}\right]^{1/5} t^{2/5},$$

$$W_c \approx \left[\frac{\pi(1-\sigma^2)^4Q\gamma_s^2}{E^2}\right]^{1/5} t^{1/5} \quad \text{and} \quad P_c \approx \left[\frac{\pi^4(1-\sigma^2)E^2\gamma_s^3}{Q}\right]^{1/5} t^{-1/5}, \tag{B 8}$$

Finally, we can now compare the scaling results and the detailed calculations of the asymptotic solutions, which suggests that

$$R(t) = \left(\frac{3\pi}{2}\right)^{2/5} R_c, \quad w(0,t) = \left(\frac{48}{\pi^4}\right)^{1/5} W_c \quad \text{and} \quad p_s(t) = \left(\frac{2}{3\pi}\right)^{1/5} P_c. \tag{B 9}$$

The crack shape (B 7) can also be written in terms of the characteristic scales:

$$\frac{w(r,t)}{W_c} = \left(\frac{64}{3\pi^6}\right)^{1/5} \left[\left(\frac{3\pi}{2}\right)^{4/5} - \left(\frac{r}{R_c}\right)^2\right]^{1/2}, \tag{B 10}$$

which can be used to compare with the experimental data in figure 4*b*.

Appendix C. Examination of the effect of the needle size

The size effects of the injection needle are not considered in the scaling laws (table 2). We experimentally investigated the effect of the needle size. For the similar parameter regimes described in §4a, a set of experiments with different needle sizes was conducted, and very good data collapse (figure 7) was observed based on the toughness scaling laws (table 2). Thus, the needle size does not appear significant in our experiments and does not influence the scaling laws.

References

1. Abé H, Mura T, Keer LM. 1976 Growth rate of a penny-shaped crack in hydraulic fracturing of rocks. *J. Geophys. Res. Solid Earth* **81**, 5335–5340. (doi:10.1029/JB081i029p05335)
2. Spence A, Sharp P. 1985 Self-similar solutions for elastohydrodyamic cavity flow. *Proc. R. Soc. A* **400**, 289–313. (doi:10.1098/rspa.1985.0081)
3. Detournay E. 2016 Mechanics of hydraulic fractures. *Annu. Rev. Fluid Mech.* **48**, 311–339. (doi:10.1146/annurev-fluid-010814-014736)
4. Lister JR, Kerr RC. 1990 Buoyancy-driven fluid fracture: similarity solutions for the horizontal and vertical propagation of fluid-filled cracks. *J. Fluid Mech.* **217**, 213–239. (doi:10.1017/S0022112090000696)
5. Lister JR, Kerr RC. 1991 Fluid-mechanical models of crack propagation and their application to magma transport in dykes. *J. Geophys. Res.* **96**, 10 049–10 077. (doi:10.1029/91JB00600)
6. Rubin AM. 1995 Propagation of magma-filled cracks. *Annu. Rev. Earth Planet. Sci.* **23**, 287–336. (doi:10.1146/annurev.ea.23.050195.001443)
7. Khristianovic SA, Zheltov YP. 1955 Formation of vertical fractures by means of highly viscous liquid. In *Proc. 4th World Petrol. Congr., Rome, Italy, 6–15 June*, vol. 2, pp. 576–586. Rome, Italy: Carlo Colombo Publishers.
8. Savitski AA, Detournay E. 2002 Propagation of a penny-shaped fluid-driven fracture in an impermeable rock: asymptotic solutions. *Int. J. Solids. Struct.* **39**, 6311–6337. (doi:10.1016/S0020-7683(02)00492-4)
9. Gor G, Stone HA, Prévost J. 2013 Fracture propagation driven by fluid outflow from a low-permeability aquifer. *Transp. Porous Media* **100**, 69–82. (doi:10.1007/s11242-013-0205-3)
10. Peirce AP. 2015 Modeling multi-scale processes in hydraulic fracturing propagation using the implicit level set algorithm. *Comput. Methods Appl. Mech. Eng.* **283**, 881–908. (doi:10.1016/j.cma.2014.08.024)
11. Hubbert MK, Willis DG. 1957 Mechanics of hydraulic fracturing. *Pet. Trans. (AIME)* **210**, 239–257.
12. Takada A. 1990 Experimental study on propagation of liquid-filled crack in gelatin: shape and velocity in hydrostatic stress condition. *J. Geophys. Res.* **90**, 8471–8481. (doi:10.1029/JB095iB06p08471)
13. Menand T, Tait SR. 2002 The propagation of a buoyant liquid-filled fissure from a source under constant pressure: an experimental approach. *J. Geophys. Res. Solid Earth* **107**, ECV 16-1–ECV 16-14. (doi:10.1029/2001JB000589)

14. Kavanagh JL, Menand T, Sparks RSJ. 2006 An experimental investigation of sill formation and propagation in layered elastic media. *Earth Planet. Sci. Lett.* **245**, 799–813. (doi:10.1016/j.epsl.2006.03.025)

15. Bunger AP, Detournay E. 2008 Experimental validation of the tip asymptotics for a fluid-driven crack. *J. Mech. Phys. Solids* **56**, 3101–3115. (doi:10.1016/j.jmps.2008.08.006)

16. Jeffrey RG, Bunger AP. 2009 A detailed comparison of experimental and numerical data on hydraulic fracture height growth through stress contrasts. *SPE J.* **14**, 413–422. (doi:10.2118/106030-PA)

17. Lai CY, Zheng Z, Dressaire E, Wexler JS, Stone HA. 2015 Experimental study on penny-shaped fluid-driven cracks in an elastic matrix. *Proc. R. Soc. A* **471**, 20150255. (doi:10.1098/rspa.2015.0255)

18. Johnson DE, Cleary MP. 1991 Implications of recent laboratory experimental results for hydraulic fractures. In *SPE 21846, presented at the 1991 SPE Rocky mountain region meeting and low permeability reservoirs symposium, Denver, April 15–17*. Richardson, TX: Society of Petroleum Engineers.

19. De Pater CJ, Cleary MP, Quinn TS, Barr DT, Johnson DE, Weijers L. 1994 Experimental verification of dimensional analysis for hydraulic fracturing. *SPE Prod. Facil.* **9**, 230–238. (doi:10.2118/24994-PA)

20. Bunger AP. 2006 A photometry method for measuring the opening of fluid-filled fractures. *Meas. Sci. Technol.* **17**, 3237–3244. (doi:10.1088/0957-0233/17/12/006)

21. Rice JR. 1968 Mathematical analysis in the mechanics of fracture. In *Chapter 3 of fracture: an advanced treatise* (ed. H Liebowitz). New York, NY: Academic Press.

22. Irwin GR. 1957 Analysis of stresses and strains near the end of a crack traversing a plate. *J. Appl. Mech.* **24**, 361–364.

23. Lucantonio A, Noselli G, Trepat X, DeSimone A, Arroyo M. 2015 Hydraulic fracture and toughening of a brittle layer bonded to a hydrogel. *Phys. Rev. Lett.* **115**, 188105. (doi:10.1103/PhysRevLett.115.188105)

24. Kavanagh JL, Menand T, Daniels KA. 2013 Gelatine as a crustal analogue: determining elastic properties for modelling magmatic intrusions. *Tectonophysics* **582**, 101–111. (doi:10.1016/j.tecto.2012.09.032)

25. Long R, Hall MS, Wu M, Hui CY. 2011 Effects of gel thickness on microscopic indentation measurements of gel modulus. *Biophys. J.* **101**, 643–650. (doi:10.1016/j.bpj.2011.06.049)

26. Di Giuseppe E, Funiciello F, Corbi F, Ranalli G, Mojoli G. 2009 Gelatins as rock analogs: a systematic study of their rheological and physical properties. *Tectonophysics* **473**, 391–403. (doi:10.1016/j.tecto.2009.03.012)

27. Bunger AP, Gordeliy E, Detournay E. 2013 Comparison between laboratory experiments and coupled simulations of saucer-shaped hydraulic fractures in homogeneous brittle-elastic solids. *J. Mech. Phys. Solids* **61**, 1636–1654. (doi:10.1016/j.jmps.2013.01.005)

28. Sneddon IN. 1951 *Fourier transforms*. New York, NY: McGraw-Hill.